Spin-orbit effects in aluminum photoionization

Gregory Miecznik and Chris H. Greene
Department of Physics and Joint Institute for Laboratory Astrophysics, University of Colorado, Boulder, Colorado 80309-0440

F. Robicheaux
Department of Physics, Auburn University, Auburn, Alabama 36849-5311
(Received 29 June 1994)

The eigenchannel R-matrix approach, in conjunction with the multichannel quantum-defect theory and the $LS \rightarrow jj$ recoupling frame transformation, is used to calculate the photoionization spectrum of Al I below the $3s3p\,^1P^o$ ionization threshold (photon energies in the range $0.44 \leq \hbar\omega \leq 0.98$ Ry). Relativistic channel mixing is incorporated in the calculations by a recoupling frame transformation and by the inclusion of experimental fine-structure threshold energies. This mixing enables autoionization of resonances whose decay would otherwise be forbidden in the pure LS-coupling scheme. The calculated J-dependent energies and widths agree well with those of experimental resonances. The complicated relativistic spectrum, with up to 11 interacting channels, provides an experimentally realizable testing ground for studies of statistical properties of resonances. The spectrum below the $3s3p\,^3P^o$ ionization threshold exhibits the Wigner and Porter-Thomas distributions of positions and widths of resonances, respectively. While portions of the aluminum spectrum appear to be random, according to these measures, there remains much underlying regularity in the level spacing and width distributions.

PACS number(s): 32.80.Fb, 31.15.+w, 32.30.−r, 05.45.+b

I. INTRODUCTION

In this paper we present results for the photoionization spectrum of aluminum up to the $3s3p\,^1P^o$ ionization threshold, utilizing the eigenchannel R-matrix approach [1,2] for many-electron atoms [3]. Calculations of the short-range scattering parameters are entirely restricted to a nonrelativistic approximation, whereas the relativistic effects are incorporated in the outer region [multichannel quantum-defect theory (MQDT) part of the calculations]. To this purpose we use the $LS \rightarrow jj$ recoupling frame transformation [4,5]. This involves both a rotation of the short-range K matrix into the jj-coupled representation and the use of experimental fine-structure splittings of the $3s3p\,^3P^o$ ionic state. The $LS \rightarrow jj$ frame transformation predicts that relativistic effects will be observable in the total cross section only in the energy range below the $3s3p\,^3P^o_2$ ionization threshold.

Several calculations of aluminum photoionization have appeared in the literature, but all have been strictly nonrelativistic. One often expects the nonrelativistic approximation to be adequate at low energies, i.e., up to states with principal quantum numbers $n \leq 10$ relative to the $3s3p\,^3P^o_{J_c}$ ionization thresholds. This usually suffices for the interpretation of low-resolution experimental spectra; in this energy range the aluminum spectrum is dominated by very broad $3s3p(\,^3P)np\,^2D^e$ resonances, which interact strongly with the $3s^2\epsilon d\,^2D^e$ continuum [6–8]. The recent calculations of Tayal and Burke [9] and previous results [10] are in good agreement with measurements of photoionization [11] and absorption cross sections [12,13]. However, many details in the observed low-energy spectrum cannot be explained using the nonrelativistic framework. The most conspicuous effect of relativity is to induce autoionization of resonances whose decay would be forbidden in LS coupling. For instance, the $3s3p(\,^3P)np\,^2P^e_{3/2}$ and $3s3p(\,^3P)np\,^4D^e_{3/2,5/2}$ Rydberg series are predicted here to be relatively short lived, due to their strong spin-orbit interaction with closed channels of the $^2D^e_J$ symmetries. We also find that the same channel interaction is responsible for a reduction of autoionizing widths for the $3s3p(\,^3P^o)np\,^2D^e_{3/2}$ levels, which were not resolved in the experimental spectra. Relativity is expected to play an important role in photoionization and also in other processes such as, for example, dielectronic recombination in electron-Al^+ scattering. Because these results may be important in many different contexts, we tabulate the positions and widths of ~ 50 of the broadest excited states and compare them with the experimental data where possible.

The energy range above $n = 10$ and below the $3s3p\,^3P^o_2$ threshold is characterized by a nonperturbative interplay of the Coulombic and relativistic interactions. Neither the measurements of the absorption and photoionization cross section nor the electron-impact experiments [14] carried out to date have been able to provide much insight into the structure and the dynamics of highly excited, autoionizing Rydberg states of aluminum. Our main objective in this paper is therefore to analyze the electron dynamics in this energy range. We will be mostly concerned with extracting regularities in the channel interactions, in part by studying Lu-Fano plots for the autoionizing states.

Another goal is to go beyond the usual calculations

of "quantum chaos." (This portion of our analysis borrows much of its viewpoint and methodology from an earlier similar study of beryllium photoionization by Greene and Aymar [15].) The spectrum exhibits "random" behavior when viewed using two popular statistical measures: the Wigner and Porter-Thomas distributions of level spacings and widths, respectively [16]. These two measures are common to all systems with quantum chaos and to random systems; therefore, these distributions tell us very little about the quantum dynamics of a specific system. In this paper, we show that it is possible to go beyond the two usual descriptions of spectra (i.e., plotting the cross section and finding the statistical properties of the levels) to obtain a more complete characterization of the dynamics. (It is often forgotten that deterministic chaos is distinct from randomness and noise and that deterministic chaos implies that there is an underlying simplicity that governs the dynamics; such simplicity and regularity can and should be explored when possible.) We attribute the properties of the resonances to the large number of interleaved Rydberg series converging to different fine-structure J_c levels of the residual $3s3p\,^3P^o$ ion. Although the random behavior emerges clearly in this spectrum, a detailed analysis shows distinct regularities in the progression of energy levels and widths.

II. CALCULATIONS

The photoionization of neutral aluminum from the $3s^23p\,^2P^o$ ground state, in the energy range below the $3s3p\,^1P^o$ threshold, is governed in the dipole approximation by the following transitions:

$$\begin{aligned} \mathrm{Al}(3s^23p\,^2P^o)+h\nu &\rightarrow \mathrm{Al}^+(3s^2\,^1S^e)\epsilon s\,^2S^e \\ &\rightarrow \mathrm{Al}^+(3s^2\,^1S^e)\epsilon d\,^2D^e \\ &\rightarrow \mathrm{Al}^+(3s3p^{\,3,1}P^o)\epsilon p\,^2S^e,\ ^2P^e,\ ^2D^e \\ &\rightarrow \mathrm{Al}^+(3s3p^{\,3,1}P^o)\epsilon f\,^2D^e. \end{aligned} \tag{1}$$

These channels fully describe photoionization in the nonrelativistic limit. In the relativistic treatment, spin-induced interactions will mix final states belonging to different $^{2S+1}L^e$ terms. Introducing the total angular momentum J in the designation of channels, the photoionization is described now in LSJ coupling by the following transitions:

$$\begin{aligned} {}^2P^o{}_{1/2}+h\nu &\rightarrow {}^2S^e,\ {}^2P^e,\ {}^4P^e,\ {}^4D^e && (J=1/2) \\ &\rightarrow {}^2P^e,\ {}^2D^e,\ {}^4S^e,\ {}^4P^e,\ {}^4D^e,\ {}^4F^e && (J=3/2), \\ {}^2P^o{}_{3/2}+h\nu &\rightarrow {}^2S^e,\ {}^2P^e,\ {}^4P^e,\ {}^4D^e && (J=1/2) \\ &\rightarrow {}^2P^e,\ {}^2D^e,\ {}^4S^e,\ {}^4P^e,\ {}^4D^e,\ {}^4F^e && (J=3/2) \\ &\rightarrow {}^2D^e,\ {}^2F^e,\ {}^4P^e,\ {}^4D^e,\ {}^4F^e,\ {}^4G^e && (J=5/2). \end{aligned} \tag{2}$$

The relevant states of Al^+ are the same as in (1).

Orbitals and atomic wave functions for Al^+ are obtained using the eigenchannel R-matrix method. This is becoming a standard computational technique and will only be outlined here; we refer the reader to previous works [1–3] for details. In this section we concentrate on the choice of an orbital basis set and on the application of the $LS \rightarrow jj$ frame transformation.

A. The eigenchannel approach

The R-matrix approach utilizes a variational principle for bound and continuum states of the Schrödinger equation. A region of interaction between the outermost electron and other electrons and the nucleus is partitioned into a short-range region $r \leq r_0$, where the electron dynamics is very complex and can only be treated approximately, and an outer region $r > r_0$, where the electrons move in the Coulomb potential of the screened nucleus. The size of the inner region ($r_0 = 15$ a.u.) is chosen so that it envelopes all physical ionic states introduced in (1) (by physical ionic states we mean those Al^+ states having energies equal to or below $3s3p\,^1P^o$) and the initial ground state. The variational principle leads to stable solutions $\delta E = 0$ for an exact wave function Ψ if the logarithmic derivative $\frac{d}{dr}\ln\Psi(r) = -b$ is constant on the surface $r = r_0$. The wave function Ψ is expanded in terms of basis functions y_i, $\psi_\beta(E) = \sum_i y_i C_{i\beta}(E)$. In the *eigenchannel* R-matrix approach, the variational condition imposed on the logarithmic derivative $db/dC_{i\beta}|_{r=r_0} = 0$, leads to a generalized eigenvalue problem for the expansion coefficients $C_{i\beta}$,

$$\underline{\Gamma}\mathbf{C}_\beta = b_\beta \underline{\Lambda}\mathbf{C}_\beta\ , \tag{3}$$

where β labels independent solutions and the $\underline{\Gamma}$ and $\underline{\Lambda}$ matrices are $\Gamma_{ij} = 2\langle y_i|E-H|y_j\rangle - \langle\langle y_i|\partial/\partial n|y_j\rangle\rangle$ and $\Lambda_{ij} = \langle\langle y_i|y_j\rangle\rangle$, respectively. Here the double bra-ket notation implies an integration over the surface of the reaction volume. Since the basis functions $\{y\}$ do not *a priori* satisfy the variational conditions, the constraint $\partial y/\partial n|_{r=r_0} = -by$ is imposed when solving the set of equations (3). The basis set $\{y\}$ is constructed as a sum of products of one-electron spin orbitals $u = \frac{1}{r}P_{nl}Y_{lm_l}\chi_{m_s}$, which can include either closed-type $[P_{nl}(r_0) = 0]$ or open-type radial orbitals $[P_{nl}(r_0) \neq 0]$; the latter are needed to permit escape of a photoelectron beyond the reaction volume into an excited Rydberg or a continuum state. Section II B describes in detail how the sets of orbitals $\{u\}$ and basis functions $\{y\}$ are constructed.

A *streamlined* version of the eigenchannel method [17] is adopted in our calculations. The $\{y\}$ set is partitioned into a subspace of closed-type basis functions and another subspace of open-type basis functions. The closed subspace is first prediagonalized and the eigenvalue problem (3) is solved in this new representation, which considerably reduces computational effort when short-range

MQDT parameters, e.g., the short-range reaction matrix, must be calculated at many energies.

This method produces nonrelativistic wave functions inside the reaction volume. In the outer region the Schrödinger equation is solved "exactly" (except for the neglect of weak multipole couplings) using standard Coulomb functions in conjunction with MQDT [18]. The inner- and outer-region solutions and their radial derivatives are matched at the boundary $r = r_0$. Section II C shows how the resulting short-range matrix is then used, together with the recoupling frame transformation, to calculate either the nonrelativistic or the relativistic cross section.

B. Choice of the orbital and configuration basis

In this paper we consider relatively soft photons whose energies are sufficient to excite only outer $3s$ and $3p$ electrons. Therefore, aluminum is treated as a system with three valence electrons outside a $1s^2 2s^2 2p^6\ {}^1S^e$ core that is common to all configurations. Effects of the closed shells on the valence electrons, including the effect of the core polarization, are taken into account by introducing a one-electron model potential $V_{\rm eff}$ [3,19]

$$H = \sum_i \frac{p_i^2}{2} + V_{\rm eff}(r_i) + \sum_{i<j} \frac{1}{r_{ij}} - 2\sum_{i<j} P_1(\cos\theta_{ij})\,[V_{\rm pol}(r_i)V_{\rm pol}(r_j)]^{1/2}\,,$$

$$V_{\rm eff}(r) = -\frac{3+10e^{-\alpha_1^l r}}{r} - \alpha_2^l e^{-\alpha_3^l r} + V_{\rm pol}(r)\,, \qquad (4)$$

$$V_{\rm pol}(r) = -\frac{\alpha_d\left[1-e^{-(r/r_c)^3}\right]^2}{2r^4}.$$

The dipole polarizability of Al^{3+}, $\alpha_d = 0.2649$ a.u., used in the polarization potential $V_{\rm pol}$, is obtained from Ref. [20]. The cutoff radius r_c and the other model-potential parameters α_i^l are fitted to experimental energies [21] of Al^{2+} and are displayed in Table I. For each angular momentum we include up to nine closed-type orbitals and one open-type orbital (the model potential is independent of the principal quantum number). This *primitive* basis set is then used to construct Al^+ states. Each is represented as a linear combination of configurations involving single and double electron excitations from reference states ($3s^2\ {}^1S^e$, $3s3p\ {}^3P^o$, and $3s3p\ {}^1P^o$) to a set of s, p, d, f, and g orbitals, preserving the spin-angular couplings and the parity of the reference terms.

Table II shows the energies of the ionic states obtained with the primitive basis set. Agreement with experiment [21] is reasonably good (no more than 1% deviation), although a large number of basis functions (about 400 for the three physical states of Al^+) were included in the calculations. In order to improve the convergence we utilized an approach with natural orbitals, which proved to be very successful in earlier R-matrix calculations [3]. The idea, as stated by Löwdin [22], is to construct a linear combination of radial orbitals (with the same angular momentum) that will give the fastest convergence for a given atomic state function. A fine example of how it works in atomic structure calculations is the multiconfiguration Hartee-Fock (MCHF) approach [23,24], where the variational principle (variation with respect to both radial orbitals and coefficients in the linear expansion of an atomic state function) ensures the fastest convergence within the chosen set of configurations. In our case, the natural orbitals are obtained by diagonalizing a density matrix constructed from the primitive set for the three physical states of Al^+. However, because of the limited number of primitive orbitals, the new set is ill conditioned and excited orbitals can have spurious nodes close to $r = r_0$. In order to eliminate this unphysical behavior, an artificial potential $\overline{V}_{\rm eff}$ is constructed [3],

$$\overline{V}_{\rm eff}(r) = V_{\rm eff}(r) + \frac{1-e^{-\beta_1 r}}{r} + \frac{\beta_2(1-e^{-\beta_3 r})}{r^2}\,, \qquad (5)$$

whose β_i parameters are adjusted until a radial eigensolution to the Schrödinger equation coincides with the lowest natural orbital for the s, p, and d symmetries (see Table I). This potential is next used to generate s, p, and d orbitals with higher principal quantum numbers.

Figure 1 compares primitive and natural s, p, and d radial orbitals (in the following $\overline{n}l$ denotes natural orbitals). The spectroscopic $\overline{3}s$ and $\overline{3}p$ orbitals are more diffuse than the primitive ones, which is due to an extra screening of the core by one of the electrons. This contrasts strongly with $\overline{3}d$, which is more contracted than $3d$ because it now plays a role of a correlation orbital in the main $\overline{3}p\overline{3}d$ perturber to $3s3p\ {}^{3,1}P$. Although the change in the spatial distributions of the P_{nl} radial orbitals is relatively small ($||P_{nl} - P_{\overline{n}l}|| < 0.1$), the natural-orbital basis improves agreement with experiment (see Table II) and speeds up the convergence. Table III shows a shortened wave function expansion for the three physical states of Al^+.

In the next step basis functions for the three-electron system of Al are constructed. To guarantee that all im-

TABLE I. Fitted parameters for the semiempirical potentials [Eqs. (4) and (5)].

l	α_1	α_2	α_3	r_c	β_1	β_2	β_3
s	4.90410	9.81290	3.32540	0.50020	0.39244	2.99441	0.48383
p	5.03230	9.92515	3.14366	0.50600	0.32484	1.51739	0.73063
d	4.86955	9.52136	3.84423	0.48230	0.58048	−4.28779	0.70448
f	4.11705	10.26234	4.24938	0.28054			
g	4.76540	10.33750	2.49541	1.02123			

TABLE II. Energies (cm^{-1}) of the target states relative to the ground term $3s^2\,{}^1S^e$ using different orbital basis. ΔE is an absolute deviation from the experimental energy difference. The numbers in square brackets denote reference numbers.

Source		$3s3p\,{}^3P^o$	ΔE	$3s3p\,{}^1P^o$	ΔE
Experiment	[21]	37516		59850	
Present	Natural	37506	10	59921	71
	Primitive	37618	102	60178	328
Other	[8]	36125	1390	60158	308
	[10]	35550	1966	59445	405

TABLE III. Shortened wave function expansion for the three physical ionic states of Al^+ in the natural-orbital basis. The numbers correspond to weights of relevant components in the expansion.

$3s^2\,{}^1S^e$		$3s3p\,{}^3P^o$		$3s3p\,{}^1P^o$	
$3s^2$	0.94965	$3s3p$	0.98985	$3s3p$	0.93285
$3p^2$	0.04480	$3s4p$	0.00200	$3s4p$	0.00655
$3d^2$	0.00086	$3p3d$	0.00816	$3s5p$	0.00201
$3p4p$	0.00303			$3p3d$	0.05710
$3p5p$	0.00141			$3p4d$	0.00149
$3d4d$	0.00025				

portant collective effects associated with the electron dynamics are accounted for (i.e., radial relaxation of orbitals, correlation, spin, and orbital polarization), we first select those components whose weight in the expansion for the three physical ionic states is at least 0.001. To this condensed set we attach an extra s, p, d, f, or g orbital and generate all final-state symmetries introduced in (2). We also add those three-electron terms needed to represent polarization of the ionic states and those which directly couple the initial and final symmetries via the electric dipole operator. The ionization energy of the $3p$ electron obtained with this basis set is 48 256 cm^{-1}, which is only 23 cm^{-1} less than the experimental value of Ref. [21].

C. MQDT and the $LS \rightarrow jj$ frame transformation

Outside the reaction volume ($r \geq r_0$) the wave function is represented in terms of the short-range $\underline{K}$ matrix as

$$\Psi_i^{(LS)} = \mathcal{A} r^{-1} \sum_j \Phi_j^{(LS)}(\omega)[f_j(r)\delta_{ij} - g_j(r)K_{ij}^{(LS)}], \quad (6)$$

where the channel function $\Phi_j(\omega)$ is a vector-coupled product of the ionic states and the spin-angular part of the outer orbital. $f_j(r)$ and $g_j(r)$ are regular and irregular Coulomb functions, respectively. In the above equation the (LS) designation is introduced as a reminder that $\underline{K}$ is block diagonal in the LS-coupled representation. $\underline{K}^{(LS)}$ is obtained by matching the solutions (6) at $r = r_0$ to the variational inner-region solutions (3). It is generally a smooth function of energy, except for a few isolated poles, which can correspond in some cases to the lowest-lying resonances confined deeply within the reaction volume. In the present case we have detected only one such pole at $\hbar\omega = 0.474$ Ry, which is associated with the $3s3p^2\,{}^2S^e$ resonance. The short-range $\underline{K}$ matrix can depend somewhat on the size of the R-matrix box, especially for energies far below the ionization thresholds. Nevertheless, the dynamics in the asymptotic region is largely independent of r_0, provided the convergence is adequate and r_0 is large enough to contain the physical ionic states and the initial $3s^2 3p\,{}^2P^o$ state.

For energies above $3s3p\,{}^1P^o$ all channels are open and the final-state wave functions are described by Eq. (6). At lower energies some channels are closed and these solutions are unphysical since $f(r)$ and $g(r)$ are asymptotically divergent for negative energies. These divergent terms are eliminated by taking an appropriate linear combination of solutions (6), which modifies the $\underline{K}$ matrix into the form [18]

$$\underline{K}^{\text{phys}} = \underline{K}^{oo} - \underline{K}^{oc}(\underline{K}^{cc} + \tan \pi\underline{\nu})^{-1}\underline{K}^{co}\,, \quad (7)$$

$$\underline{\nu}_{ij} = \delta_{ij}\nu_j. \quad (8)$$

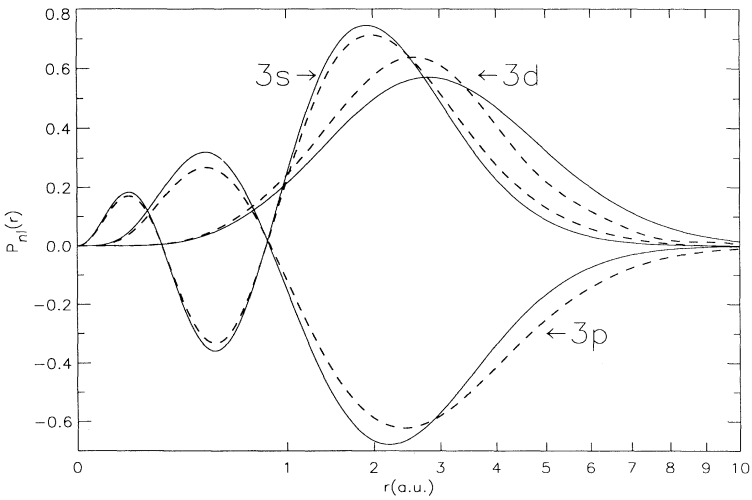

FIG. 1. Radial functions $P_{nl}(r)$ for the $3s$, $3p$, and $3d$ orbitals of Al are shown (on a scale evenly distributed in $\sqrt{r}$) in the primitive-orbital basis (solid lines) and in the natural-orbital basis (dashed lines).

ν_j is an effective quantum number associated with a threshold energy E_j via relation $\nu_j = 1/\sqrt{2(E_j - E)}$ and subscripts o and c refer to the open- and closed-channel subspaces of $\underline{K}$, respectively. A similar transformation is also applied to the reduced dipole-matrix elements connecting the initial and final states [18].

At this point all calculations have been performed in the nonrelativistic fashion, assuming pure LS coupling; the only exception is the fact that the experimental energies of Al^{2+} were used to determine the orbital basis. The LS-coupling scheme is adequate for aluminum within the R-matrix box, since the electrostatic forces are much stronger than the spin-induced interactions and a mixing between ionic states of Al^+ corresponding to different $^{2S_c+1}L_c^o$ terms is thus negligible. However, this approximation breaks down if we move sufficiently far beyond the reaction zone, because the energy of the escaping electron depends not only on the L_c and S_c quantum numbers, but also on the total spin-angular momentum J_c of the residual ion. To account for the fine-structure splitting of a $^{2S_c+1}L_c^o$ term, the spin and orbital angular momentum of the core are first coupled to form an intermediate J_c vector, but the final coupling with an outer electron (for which we reserve the l_o, $s_o = \frac{1}{2}$, and j_o quantum numbers) is, however, somewhat arbitrary. In our work we use the jj-coupled representation $|[(L_c, S_c)J_c, (l_o, s_o)j_o]J\rangle$, although any coupling scheme diagonal in J_c would be equally valid.

The $LS \rightarrow jj$ recoupling frame transformation involves a real orthogonal recoupling matrix $\underline{T}$, which is proportional to a 9-j symbol. This induces a transformation of the final-state wave functions and of the short-range $\underline{K}$ matrix:

$$\Psi^{(jj)} = \Psi^{(LS)}\underline{T}^{\dagger} , \tag{9}$$

$$\underline{K}^{(jj)} = \underline{T}\underline{K}^{(LS)}\underline{T}^{\dagger}. \tag{10}$$

A final aspect is equally important, namely, in the MQDT calculations, the effective quantum numbers ν [in $\tan \pi\underline{\nu}$ of Eq. (7)] must be calculated using experimental fine-structure thresholds. Once the short-range $\underline{K}^{(jj)}$ matrix has been constructed, the elimination of divergent solutions proceeds in the same way described by Eq. (7).

Reference [25] points out how the effect of the fine-structure splitting ΔE_{J_c} on the autoionizing spectrum can be understood in terms of a cumulative J_c-dependent change in the phase of the outer electron. This phase difference increases with r roughly as $r^{3/2}\Delta E_{J_c}$. Since the splitting between the lowest $J_c = 0$ and the highest $J_c = 2$ fine-structure levels of the $3s3p\,^3P^o$ term is about 8×10^{-4} a.u., the phase difference becomes appreciable only at large values of $r \geq 100$ a.u. Thus only an electron that escapes beyond ≈ 100 bohr radii in one of channels corresponding to the $3s3p\,^3P^o_{J_c}$ thresholds experiences nonperturbative relativistic effects. This condition translates into effective quantum numbers in the range $\nu > 10$. The effects of relativity can also be understood by studying the energy dependence of $\underline{K}^{\rm phys}$. Consider only the subspace of $\underline{K}^{cc}$ associated with channels attached to the $3s3p\,^3P^o_{J_c}$ thresholds. (We can assume here that channels converging to the higher $3s3p\,^1P^o$ threshold have been previously eliminated using a contracted $\underline{K}_{\rm contr}$ matrix instead of the full $\underline{K}$ matrix [18]. In the present case the contracted matrix varies smoothly with energy because there are no perturbers converging to higher thresholds below $3s3p\,^3P^o_2$.) At low energies, the fine-structure splitting of the ionic states affects ν_j in the following way:

$$\nu_j(E) = \nu_{\rm av}(E)\left(1 - \frac{1}{2}\frac{\Delta E_j}{E_{\rm av} - E} + \cdots\right) , \tag{11}$$

where the subscript av denotes either the energy or else the effective quantum number corresponding the $3s3p\,^3P^o$ threshold, statistically averaged over the J_c levels. At energies where $\Delta E_j/(E_{\rm av} - E) \ll 1$, i.e., well below the thresholds, $\tan \pi\underline{\nu}$ is proportional to the identity matrix and it therefore commutes with $\underline{K}^{cc}$. Thus any orthogonal transformation of $\underline{K}^{cc}$ leaves the eigenvalues of $(\underline{K}^{cc} + \tan \pi\underline{\nu})$ unchanged. Consequently, at low energies, the $LS \rightarrow jj$ transformation amounts to a pure rotation of channel functions, with absolutely no effect on the dynamics of the system. At energies just below the $3s3p\,^3P^o_{J_c}$ thresholds, however, the effective quantum numbers ν_j associated with different J_c levels are very different from $\nu_{\rm av}$ and the $LS \rightarrow jj$ recoupling frame transformation will have a nonperturbative effect on the electron dynamics.

The frame transformation has proved to be very successful in earlier studies (see [26] and references cited therein) and is also expected to be accurate in the present problem, but it does have some limitations. The relativistic interaction, which is incorporated in this approximation, couples only closed channels converging to the same $^{2S_c+1}L_c$ thresholds (except for $L_c = 0$ or $S_c = 0$), implying that all decay into the continua is induced by the Coulomb r_{ij}^{-1} operator. In other words, the frame transformation neglects all spin-related interactions that directly couple the closed and open channels. One way to account for these interactions is to introduce the spin-orbit operators directly into the Hamiltonian [26], e.g., using perturbation theory. An alternative method, presented in Ref. [3], is to build in the intermediate coupling of Al^+ functions having the same J_c, but different $^{2S_c+1}L_c$ terms.

III. RESULTS

A. Low-energy spectra below $3s3p\,^3P^o_2$: Cross sections

Figures 2(a) and 2(b) show the photoionization cross sections σ in the energy region between the $3s^2\,^1S^e$ and $3s3p\,^3P^o$ thresholds. The total cross section $\sigma_{\rm av}$ in Fig. 2(a) is a weighted sum of cross sections obtained for each initial $3s^23p\,^2P^o_J$ level, i.e., $\sigma_{\rm av} = \frac{1}{3}\sigma(^2P^o_{1/2}) + \frac{2}{3}\sigma(^2P^o_{3/2})$, where we assumed a statistical mixture of the two initial J levels, and is plotted as a function of photon energy above the ground level $3s^23p\,^2P^o_{1/2}$. The cross section $\sigma(^2P^o_{3/2})$ in Fig. 2(b) is obtained for the initial

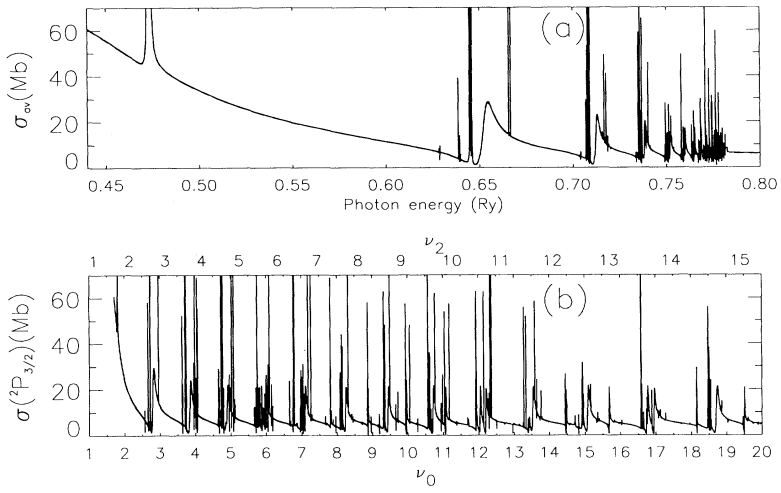

FIG. 2. The total photoionization cross section σ of aluminum is plotted between the $3s^2\,{}^1S^e$ and $3s3p\,{}^3P^o_{J_c}$ ionization thresholds. Relativistic effects are incorporated using the $LS \rightarrow jj$ frame transformation. The length and velocity gauge cross sections are plotted on both (a) and (b), but they nearly coincide. In (a) we assume a statistical mixture of the ${}^2P^o_{1/2}$ and ${}^2P^o_{3/2}$ levels for the initial term $3s^23p\,{}^2P^o$, i.e., $\sigma_{\rm av} = \frac{1}{3}\sigma({}^2P^o_{1/2}) + \frac{2}{3}\sigma({}^2P^o_{3/2})$. The photon energy is relative to $3s^23s\,{}^2P^o_{1/2}$. In (b) the cross section $\sigma({}^2P^o_{3/2})$ obtained from the initial $3s^23p\,{}^2P^o_{3/2}$ level is plotted versus effective quantum numbers relative to the $3s3p\,{}^3P^o_0$ threshold (lower axis) and relative to $3s3p\,{}^3P^o_2$ (upper axis).

level $3s^23p\,{}^2P^o_{3/2}$ and is plotted versus effective quantum numbers relative to the $3s3p\,{}^3P^o_0$ and $3s3p\,{}^3P^o_2$ ionization thresholds of Al^+. In the calculation of threshold energies of Al^+ we used experimental energies from Ref. [21]. They are 0.439 952, 0.780 694, 0.781 256, 0.782 400, and 0.985 344 Ry for the $3s^2\,{}^1S^e_0$, $3s3p\,{}^3P^o_{0,1,2}$, and $3s3p\,{}^1P^o_1$ levels, respectively, and the fine-structure splitting of the ground term $3s^23p\,{}^2P^o$ is 1.0210×10^{-3} Ry.

At low energies ($\hbar\omega \leq 0.75$ Ry) the cross section is dominated by a series of broad $3s3p({}^3P)np\,{}^2D^e$ resonances. The unusually large cross section at the $3s^2\,{}^1S^e$ threshold (61 Mb) and right above it is attributed to the presence of the $3s3p^2\,{}^2D^e$ perturber, which is diluted among the $3s^2nd\,{}^2D^e$ bound states and the continuum $3s^2\epsilon d\,{}^2D^e$ [6–8]. No particular energy level can be assigned to the $3s3p^2\,{}^2D^e$ term.

The lowest narrow resonance at $\hbar\omega = 0.474$ Ry corresponds to the $3s3p^2\,{}^2S^e$ state, while the next few broad resonances are the $3s3p({}^3P)np\,{}^2D^e$ series. The $3s3p({}^3P)np\,{}^2S^e$ and $3s3p({}^3P)nf\,{}^2D^e$ resonances give rise to sharp peaks in the spectrum. So do resonances like $3s3p({}^3P)np\,{}^2P^e$ and $3s3p({}^3P)np\,{}^4D^e$ (for $n < 10$), which cannot autoionize in a strict LS approximation, but appear in the spectrum owing to spin-orbit mixing with channels of the ${}^2D^e$ symmetry. Aside from specific spin-orbit effects, which we discuss in the following subsection, the cross section in Fig. 2(a) agrees reasonably well over the entire region with the nonrelativistic cross section calculated by Tayal and Burke [9]. Our cross section at the $3s^2\,{}^1S^e$ threshold is 61 Mb, compared to 55 Mb obtained by Tayal and Burke, and the measured value of 65 ± 7 Mb by Roig [13]. Our velocity and length gauge calculations differ on average by only 1%.

B. Low-energy spectra below $3s3p\,{}^3P^o_2$: Classification of resonances

Table IV summarizes positions, and full widths at half maximum, of the $3s3p({}^3P)np\,{}^2S^e$ resonances with effective quantum numbers $\nu < 10$. They are found by searching for maxima of the energy derivative of the eigenphase sum. In this energy range, where the relativistic effects have a perturbative character, we can compare our results with other data, where it is available. The resonance positions are in very good agreement with the experimental [13] and other theoretical [9] data and de-

TABLE IV. Energies (above $3s^23p\,{}^2P^o_{1/2}$), widths, and effective quantum numbers ν (relative to the $3s3p\,{}^3P^o_2$ threshold, after Roig [13]) of some $3s3p({}^3P)np\,{}^2S^e$ resonances. The $z[n]$ notation implies $z \times 10^n$.

	Energy (Ry)			Width (Ry)			$\nu({}^3P^o_2)$	
State	Present	Other[a]	Expt.[b]	Present	Other	Expt.[b]	Present	Expt[b]
$3p\,{}^2S$	0.4737	0.4686	0.4716	3.25[-4]	1.74[-4]	3.11[-4]	1.7998	1.7937
$4p\,{}^2S$	0.6666	0.6651	0.6657	5.77[-6]	4.90[-5]		2.9386	2.9272
$5p\,{}^2S$	0.7176	0.7177	0.7175	2.63[-6]	2.00[-5]		3.9307	3.9273
$6p\,{}^2S$	0.7410	0.7422	0.7410	1.89[-6]	1.00[-5]		4.9202	4.9149
$7p\,{}^2S$	0.7537		0.7536	1.26[-6]			5.9043	5.8967
$8p\,{}^2S$	0.7613		0.7612	7.24[-7]			6.8852	6.8761
$9p\,{}^2S$	0.7662		0.7662	3.39[-7]			7.8634	7.8555
$10p\,{}^2S$	0.7696		0.7696	1.32[-7]			8.8362	8.8395

[a]Reference [9].
[b]Reference [13].

viations in the present and experimental quantum defects are at worst 0.01. Our calculated autoionization width for the lowest $3s3p^2\,{}^2S^e$ resonance agrees very well with Roig's observed value, but for higher-lying states the present widths are consistently smaller than those of Tayal and Burke. No experiments performed to date can distinguish between these two calculations and it should be remembered that such small autoionization widths are very sensitive to small errors in the $\underline{K}$ matrix.

Next consider $3s3p(\,{}^3P)np\,{}^2D^e$ in Table V. This is the most prominent series in the low-energy spectrum. To emphasize the relativistic effects we show results obtained in both the nonrelativistic and relativistic calculations. In this section we use Roig's convention [13] to classify individual resonances, although it should be pointed out that the LS-coupling scheme adopted from Ref. [13] is only adequate for the lower members of this and other series converging to the $3s3p\,{}^3P^o_{J_c}$ thresholds. For the first two or three lowest-lying resonances, the fine-structure levels $^2D^e_{3/2}$ and $^2D^e_{5/2}$ almost overlap and their widths are virtually identical to the widths obtained in the nonrelativistic calculation. For higher states ($n > 6$), however, we see a considerable difference between the two fine-structure levels; the relevant quantum defects are different by about 0.1 and the $^2D^e_{3/2}$ levels are an order of magnitude narrower than the $^2D^e_{5/2}$ levels. Such a reduction of widths indicates a strong J-dependent mixing; we found that the $^2D^e_{3/2}$ channels are very strongly mixed with the $^2P^e_{3/2}$ channels. Since the $3s3p(\,{}^3P)np\,{}^2P^e$ states cannot autoionize via the direct Coulomb interaction, the spin-orbit interaction enhances the decay rate of the $^2P^e_{3/2}$ levels (see Table VI), while it simultaneously reduces the widths of the $^2D^e_{3/2}$ levels. This is consistent with Roig's experiment, where only relatively pure $3s3p(\,{}^3P)np\,{}^2D^e_{5/2}$ levels were resolved in the low-energy spectrum.

Positions, widths, and compositions of the $3s3p(\,{}^3P)np\,{}^2P^e_{3/2}$ levels are shown in Table VI. It is instructive to follow changes in the widths which, in contrast to the general rule $\Gamma \sim \nu^{-3}$, actually *increase* as the principal quantum number increases from $n = 5$ to $n = 8$. This increase of widths is caused by an increasing admixture of the $^2D^e$ symmetry; at $n = 8$ the Rydberg series $3s3p(\,{}^3P)np\,{}^2P^e_{3/2}$ and $3s3p(\,{}^3P)np\,{}^2D_{3/2}$ have an avoided crossing and they interchange in character. Good agreement is achieved between resonance positions and the experimental results; the difference in quantum defects is only in the second digit.

Besides the $^2P^e_{3/2}$ symmetry, there are also other LS-forbidden symmetries which autoionize relatively fast, at least faster than the LS-allowed $3s3p(\,{}^3P)np\,{}^2S^e$ series. This is due to both the relativistic mixing with the $^2D^e$ closed channel and the strong Coulomb coupling between the $3s3p(\,{}^3P)np\,{}^2D^e$ series and the $3s^2\epsilon d\,{}^2D^e$ continuum. The decay rates are, in a perturbative treatment, proportional to the square of an interaction element between the open and closed channels. Since the widths for the $^2D^e$ series are about 10^3 times larger than for $^2S^e$, an admix-

TABLE V. Energies (above $3s^2 3p\,{}^2P^o_{1/2}$), widths, and effective quantum numbers of the $3s3p(\,{}^3P)np\,{}^2D^e$ resonances below $\nu = 10$ (relative to $3s3p\,{}^3P^o_2$), obtained in both nonrelativistic and relativistic approximations. The $6p\,{}^2D^e_{5/2}$ and $7p\,{}^2D^e_{5/2}$ levels could not be accurately resolved in the spectra due to overlapping features and are left out from this table.

	Energy (Ry)			Width (Ry)			$\nu(\,{}^3P^o_2)$	
State	Present	Other[a]	Expt.[b]	Present	Other	Expt.[b]	Present	Expt.[b]
$4p\,{}^2D$	0.6531	0.6496	0.6531	6.89[-3]	1.08[-2]	7.46[-3]	2.7810	2.7650
$5p\,{}^2D$	0.7130	0.7121	0.7122	2.07[-3]	2.52[-3]	3.19[-3]	3.8093	
$^2D_{3/2}$	0.7124			2.05[-3]			3.7812	
$^2D_{5/2}$	0.7134		0.7132	2.06[-3]			3.8061	3.8031
$6p\,{}^2D$	0.7388	0.7386	0.7380	9.17[-4]	1.14[-3]	2.34[-3]	4.8157	
$^2D_{3/2}$	0.7383			8.52[-4]			4.7628	
$^2D_{5/2}$	0.7392		0.7390	8.89[-4]			4.8100	4.7994
$7p\,{}^2D$	0.7523	0.7524	$0.7527_{5/2}$	4.87[-4]	6.12[-4]		5.8163	
$^2D_{3/2}$	0.7520			3.46[-4]			5.7359	
$8p\,{}^2D$	0.7604	0.7606		2.90[-4]	6.60[-5]		6.8144	
$^2D_{3/2}$	0.7603		0.7604	2.31[-5]			6.7200	6.7354
$9p\,{}^2D$	0.7655	0.7658		1.87[-4]	1.55[-4]		7.8108	
$^2D_{3/2}$	0.7656			4.14[-5]			7.7071	
$^2D_{5/2}$	0.7660		0.7659	1.59[-4]			7.8071	7.7939
$10p\,{}^2D$	0.7690	0.7691		1.27[-4]	1.55[-4]		8.8053	
$^2D_{3/2}$	0.7692			1.87[-5]			8.6977	
$^2D_{5/2}$	0.7695		0.7695	1.02[-4]			8.8033	8.8105
$11p\,{}^2D$	0.7715			9.03[-5]			9.7984	
$^2D_{3/2}$	0.7717			4.50[-6]			9.6865	
$^2D_{5/2}$	0.7720		0.7720	6.61[-5]			9.7983	9.7942

[a]Reference [9].
[b]Reference [13].

TABLE VI. Energies, widths (both in Ry), channel decompositions [the shortened $np\,^{2S+1}L^e$ notation is used in columns 5 and 6 to designate the $3s3p(\,^3P)np\,^{2S+1}L^e$ channels], and effective quantum numbers of the $3s3p(\,^3P)np\,^2P^e_{3/2}$ Rydberg states.

	Energy		Width	Composition (%)		$\nu(\,^3P^o_2)$	
np	Present	Expt.[a]		$np\,^2P^e$	$np\,^2D^e$	Present	Expt.[a]
$4p$	0.6457	0.6448	2.31[-5]	99	0.3	2.7052	2.6963
$5p$	0.7089	0.7082	2.35[-5]	82	1	3.7181	3.6991
$6p$	0.7367	0.7364	4.41[-5]	64	4	4.7374	4.7056
$7p$	0.7511	0.7510	1.02[-4]	52	18	5.7614	5.7483
$8p$	0.7595	0.7591	1.36[-4]	30	43	6.7780	6.7195
$9p$	0.7647	0.7643	1.12[-4]	17	57	7.7841	7.6765
$10p$	0.7683	0.7681	8.05[-5]	11	60	8.7839	8.7304
$11p$	0.7708	0.7707	5.77[-5]	9	61	9.7847	9.7392

[a]Reference [13].

ture of only about 0.1% of the $^2D^e$ symmetry may cause the LS-forbidden states to autoionize faster than the relevant $^2S^e$ series. Such an enhancement of decay and recombination rates could be important, e.g., for studies of dielectronic recombination, and might be explored further. In Tables VII and VIII we show widths and channel decompositions of the $3s3p(\,^3P)np\,^4D^e_{3/2,5/2}$ series, which are the next strongest after the $3s3p(\,^3P)np\,^2P^e_{3/2}$ series. Similarly to the $3s3p(\,^3P)np\,^2P^e_{3/2}$ levels, we observe the same enhancement of widths caused by an increasing admixture of the $^2D^e$ symmetry. Agreement with the observations by Roig is very satisfactory for the $J=\frac{3}{2}$ levels, but we are consistently lower in our resonance energies. On the other hand, the $3s3p(\,^3P)np\,^4D^e_{5/2}$ levels were not resolved in the experimental spectrum, although their widths are predicted to be comparable to the widths of the $^2P^e_{3/2}$ series. The $3s3p(\,^3P)np\,^4D^e_{1/2}$ series (and other states with $J=\frac{1}{2}$) are found to be extremely narrow. This is because the $3s3p(\,^3P)np\,^2S^e$ channel, which can induce a coupling between the $J=\frac{1}{2}$ levels and the $3s^2\epsilon s\,^2S^e_{1/2}$ continuum, has a very slow autoionization rate itself. This series is omitted from our tables.

C. High-energy spectra below $3s3p\,^3P^o_2$

The relativistic effects, which are responsible for enhancement and reduction of autoionizing widths of resonances, can also be seen in the photoionization cross section in Fig. 2(b). This cross section is obtained from the $3s^23p\,^2P^o_{3/2}$ initial level and is plotted versus effective quantum numbers ν_{J_c} relative to the $3s3p\,^3P^o_{J_c}$ thresholds. At low energies ($\nu_0<8$), where the spin-orbit coupling is relatively weak, many series of very narrow resonances are superimposed on broad $3s3p(\,^3P)np\,^2D^e$ Rydberg series. In the higher-energy region, the relativistic interaction significantly increases the widths of some LS-forbidden resonances. This makes the spectrum look very complex, with many overlapping resonances of comparable widths converging to all three $3s3p\,^3P^o_{J_c}$ thresholds.

Already at energies corresponding to the $n=10$ principal quantum number we observe a considerable departure from pure LS coupling. To investigate the transition from LS to jj coupling, we analyzed the spectrum above $n=10$, in the energy range $0.77\le E\le 0.78$ Ry, just below the $3s3p\,^3P^o_0$ ionic state. Instead of classifying individual resonances, we tabulate the number of resonances

TABLE VII. Energies, widths (both in Ry), channel decompositions, and effective quantum numbers of the $3s3p(\,^3P)np\,^4D^e_{3/2}$ Rydberg states.

	Energy		Width	Composition (%)		$\nu(\,^3P^o_0)$	
np	Present	Expt.[a]		$np\,^4D^e$	$np\,^2D^e$	Present	Expt.[a]
$5p$	0.7046	0.7075	2.99[-6]	99	0.1	3.6242	3.6973
$6p$	0.7344	0.7357	5.23[-6]	96	0.4	4.6500	4.7151
$7p$	0.7496	0.7503	8.78[-6]	90	1	5.6707	5.7355
$8p$	0.7583	0.7588	1.35[-5]	79	3	6.6890	6.7676
$9p$	0.7638		1.73[-5]	65	6	7.7037	
$10p$	0.7675		1.84[-5]	54	9	8.7151	
$11p$	0.7701		1.21[-5]	35	8	9.7329	

[a]Reference [13].

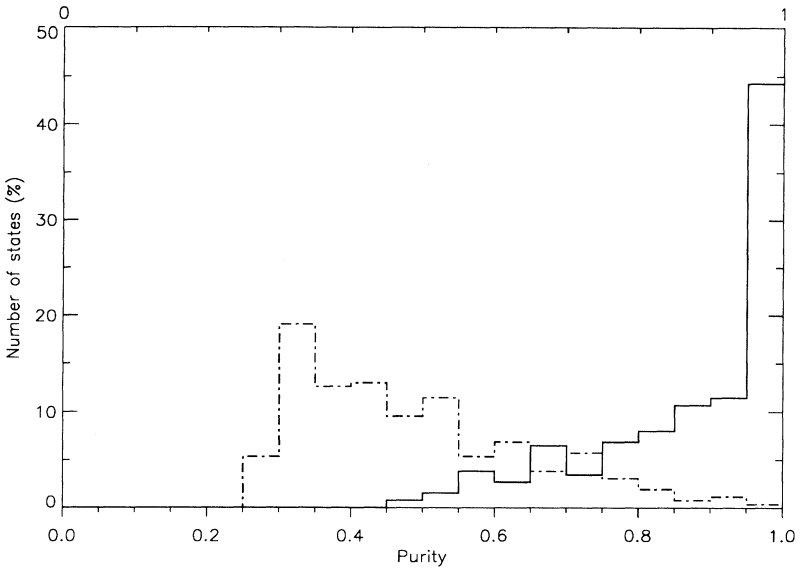

FIG. 3. Purity of the Rydberg states (obtained for photon energies in the range $0.77 \leq \hbar\omega \leq 0.78$ Ry) for the final $J = \frac{3}{2}$ symmetry in either LS coupling (dash-dotted line) or jj coupling (solid line).

having a given purity in each of the coupling schemes. In order to eliminate effects arising from an intermediate coupling, we first sum the weights of different channels corresponding to the same final ^{2S+1}L symmetry in the LS-coupling scheme. Similarly, the relativistic jj-coupled functions are first summed over the weights of those channels which have a common core $(L_c, S_c)J_c$. This reflects the fact that any final coupling between the residual ion, which is in the $(L_c, S_c)J_c$ state, and an outer electron is physically equivalent. Figure 3 shows that the relativistic coupling provides a better representation for these energies; only 1.5% of all states have purity in J_c quantum numbers worse than 50% and almost 50% of states are more than 95% pure. This is in a striking contrast to the LS-coupled channels, where none of the states has a well defined $^{2S+1}L^e$ symmetry.

D. Spectra above $3s3p\,^3P^o_2$

Above the $3s3p\,^3P^o_2$ threshold the relativistic effects on the total cross section are negligible. In our approximation the spectra plotted in Fig. 4, obtained with and without relativity coincide exactly [except that the fine-structure splitting of the ground term $3s^23p\,^2P^o$ causes an energy shift between the ionization thresholds in the cross sections $\sigma(^2P^o_{1/2})$ and $\sigma(^2P^o_{3/2})$ for the two initial levels], since the $3s3p\,^1P^o$ ionic state does not have a fine-structure splitting. The neglected mixing of the $3s3p\,^3P^o$ and $3s3p\,^1P^o$ ionic states, which is mainly responsible for the spin-induced interactions above the $^3P^o_2$ threshold, is only of order 0.1%. The dominant resonances are $3s3p(\,^1P)np\,^2D^e$, although the $3s3p(\,^1P)np\,^2S^e$ and $3s3p(\,^1P)np\,^2P^e$ series are now much more intense than the analogous series converging to the $3s3p\,^3P^o_{J_c}$ thresholds. Only two series of broad peaks are immediately apparent in our calculated photoionization spectrum in this range, whereas Tayal and Burke found three distinct series. The origin of this discrepancy can be traced to an almost perfect overlap of our $3s3p(\,^1P)np\,^2S^e$ and

TABLE VIII. Energies, widths (both in Ry), channels decomposition, and effective quantum numbers of the $3s3p(\,^3P)np\,^4D^e_{5/2}$ Rydberg states.

np	Energy	Width	Composition (%) $np\,^4D^e$	Composition (%) $np\,^2D^e$	$\nu(\,^3P^o_0)$
$5p$	0.7050	5.20[-6]	98	0.1	3.6355
$6p$	0.7349	9.26[-6]	95	0.6	4.6731
$7p$	0.7500	1.33[-5]	90	2	5.7141
$8p$	0.7588	1.59[-5]	84	3	6.7563
$9p$	0.7643	1.68[-5]	79	5	7.8108
$10p$	0.7680	1.66[-5]	75	6	8.8780

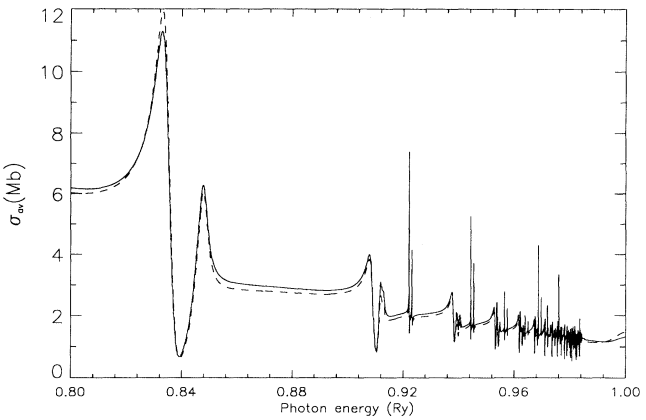

FIG. 4. The total photoionization cross sections $\sigma_{av} = \frac{1}{3}\sigma(^2P^o_{1/2}) + \frac{2}{3}\sigma(^2P^o_{3/2})$ for aluminum are shown as a function of photon energy (above $3s^23s\,^2P^o_{1/2}$) between the $3s3p\,^3P^o$ and $3s3p\,^1P^o$ ionization thresholds. In this energy range the spectrum obtained using the $LS \rightarrow jj$ frame transformation coincides with the nonrelativistic spectrum, except for an energy shift between ionization thresholds of Al^+ in $\sigma(^2P^o_{1/2})$ and $\sigma(^2P^o_{3/2})$, corresponding to the fine-structure splitting of the ground $3s^23p\,^2P^o$ term. Solid line, length gauge; dashed line, velocity gauge.

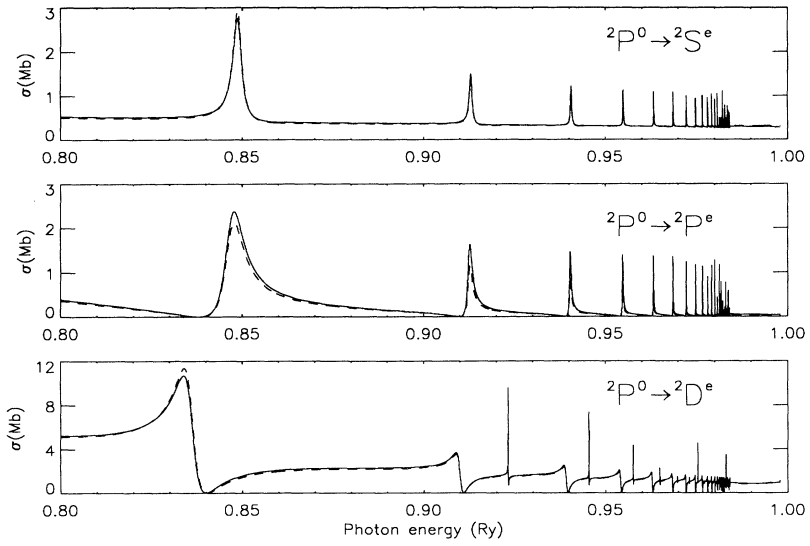

FIG. 5. The partial photoionization cross sections obtained in the nonrelativistic approximation are shown at energies between the $3s3p\,^3P^o$ and $3s3p\,^1P^o$ ionic states.

$3s3p(\,^1P)np\,^2P^e$ resonances, as can be seen from Fig. 5, where we plot nonrelativistic partial cross sections. The energy shift of ionization thresholds due to the fine-structure splitting of the ground term $3s^23p\,^2P^o$ is clearly manifested in the vicinity of narrow resonances, for example, the $3s3p(\,^1P)nf\,^2D^e$ and $3s3p(\,^1P)np\,^2S^e$, $^2P^e$ series. Except for that, there is good agreement in both the positions and widths of the resonances. The seven lowest resonances for each final-state symmetry are classified in Table IX. For the lowest-lying $3s3p(\,^1P)4p\,^2D^e$ and $3s3p(\,^1P)4p\,^2P^e$ states, which are the only states converging to $3s3p\,^1P^o$ identified in the experiment, our results disagree with the classifications presented by Roig, who found these two resonances to lie well below the $3s3p\,^3P^o_{J_c}$ thresholds, with effective quantum numbers near 2.1. To double-check the present results we performed an additional MCHF [24] calculation and found almost the same effective quantum numbers for the $3s3p(\,^1P)4p\,^2D^e$ and $3s3p(\,^1P)4p\,^2P^e$ states, 2.6 and 2.7 respectively, as obtained with the R-matrix program. This conclusions are also consistent with Le Dourneuf *et al.* [10], who found these states to have the quantum defects about 1.3. Accordingly, we suspect that these two lines observed by Roig may be due to impurities of some type.

IV. INTERPRETATION OF THE PHOTOIONIZATION CROSS SECTION

A. Regularities

Next we consider in more detail the spectrum in the energy range just below the $3s3p\,^3P^o_0$ ionization threshold, where relativistic effects are the strongest. Because of the complicated channel mixing, with up to 11 interacting channels for the $J = \frac{3}{2}$ final symmetry and numerous overlapping features, it is no longer useful to carry out a standard resonance analysis, i.e., to determine resonance positions, widths, and compositions. Instead, we will extract regularities in the perturbations of different Rydberg series.

The complexity of Rydberg channel interactions in this energy range is caused by the different time scales of electron motion in different channels associated with the three $3s3p\,^3P^o_{J_c}$ ionization thresholds. The resulting competition among these time scales can lead to extremely complicated spectra. Lu-Fano-type plots [27] can be used to extract regularities from the resulting spectra. In any

TABLE IX. Energies, widths (both in Ry), and effective quantum numbers of some $3s3p(\,^1P)np\,^{2S+1}L^e$ resonances.

	$3s3p(\,^1P^o)np\,^2D^e$			$3s3p(\,^1P^o)np\,^2P^e$			$3s3p(\,^1P^o)np\,^2S^e$		
np	E	ν	Γ	E	ν	Γ	E	ν	Γ
$4p$	0.8359	2.5869	5.65[-3]	0.8468	2.6864	6.21[-3]	0.8488	2.7065	8.01[-4]
$5p$	0.9100	3.6422	2.02[-3]	0.9125	3.7058	1.48[-3]	0.9130	3.7189	2.55[-4]
$6p$	0.9392	4.6563	9.45[-4]	0.9403	4.7107	5.61[-4]	0.9406	4.7287	1.13[-4]
$7p$	0.9542	5.6625	5.19[-4]	0.9547	5.7129	2.69[-4]	0.9549	5.7328	5.89[-5]
$8p$	0.9628	6.6663	3.15[-4]	0.9632	6.7145	1.49[-4]	0.9633	6.7349	3.44[-5]
$9p$	0.9683	7.6693	2.05[-4]	0.9685	7.7161	9.16[-5]	0.9686	7.7365	2.17[-5]
$10p$	0.9720	8.6720	1.41[-4]	0.9722	8.7179	6.04[-5]	0.9722	8.7382	1.46[-5]

multichannel Rydberg spectrum having two ionization thresholds, the quantum defect μ_1 relative to one threshold is (to an excellent approximation) a periodic function of the effective quantum number ν_2 relative to the second threshold, provided the short-range $\underline{K}$ matrix has a weak energy dependence. In our spectrum, near and below the $3s3p\,^3P_0^o$ threshold, the periodicity is lost because the number of Rydberg thresholds is larger (the spectrum between $3s3p\,^3P_0^o$ and $3s3p\,^3P_2^o$ is regular because there are no resonances at these and lower energies that converge to the $3s3p\,^1P^o$ threshold). Nevertheless, we can still expect much regularity because perturbers converging to the different thresholds still appear periodically in the appropriate effective quantum number.

The idea of Lu-Fano plots to trace regularities in the spectra is adopted in the present paper in a different way. We use an approach introduced by Greene and Aymar [15] that permits us to analyze the positions of resonances as well as their widths. In this approach, the position and width of each isolated resonance are obtained by searching for a a corresponding pole of the physical $\underline{S}^{\rm phys}$ matrix in the complex energy plane. To clarify, $\underline{S}^{\rm phys}$ is obtained by eliminating divergent terms in the complex asymptotic solutions in all closed channels c. The elimination procedure yields an equation similar to (7), i.e.,

$$\underline{S} \equiv \frac{1+i\underline{K}}{1-i\underline{K}}\ , \tag{12}$$

$$\underline{S}^{\rm phys} = \underline{S}^{oo} - \underline{S}^{oc}\left(\underline{S}^{cc} - e^{-2i\pi\underline{\nu}}\right)^{-1}\underline{S}^{co}. \tag{13}$$

Provided the greatest energy dependence arises from the diagonal matrix of effective quantum numbers ν, as is the case here, the poles of the $\underline{S}^{\rm phys}$ matrix occur at roots of the determinantal equation

$$\det|\underline{S}^{cc} - e^{-2i\pi\underline{\nu}}| = 0. \tag{14}$$

The solutions of this equation can be transcribed using the Rydberg formula into a discrete set of complex quantum defects relative to the lowest threshold $\mu_0 = {\rm Re}\mu_0 + i{\rm Im}\mu_0$. At complex energies $E = E_0 - \frac{1}{2\nu_0{}^2}$ ($\nu_0 = n - \mu_0$), we can use the Rydberg formula in the approximate form

$$E \approx E_0 - \frac{1}{2(n-{\rm Re}\mu_0)^2} - \frac{i}{2}\frac{2{\rm Im}\mu_0}{(n-{\rm Re}\mu_0)^3}, \tag{15}$$

where the imaginary term is related to the resonance width Γ by $\Gamma = 2{\rm Im}\mu_0/\nu_0^3$. This equation is accurately satisfied for states lying sufficiently close to the $J_c = 0$ ionization threshold, such that $n \gg {\rm Im}\mu_0$.

A search for exact roots of (14) must be performed numerically in general. Greene and Aymar [15] have pointed out, however, that approximate roots can be parametrized in terms of a complex quantum defect μ_0 that is continuous in the energy. The idea is to "eliminate" the upper channels in the $\underline{S}^{cc}$ matrix, i.e., to enforce exponential decay in all closed channels except those attached to the lowest closed channel threshold $3s3p\,^3P_0^o$. As discussed in Ref. [15], Eq. (14) can be transformed into the following set of linear equations:

$$\underline{S}_a^{\rm red}\mathbf{A}_a = e^{-2i\pi\underline{\nu}_a}\mathbf{A}_a\ , \tag{16}$$

$$\underline{S}_a^{\rm red} = \underline{S}_{aa} - \underline{S}_{ab}\left(\underline{S}_{bb} - e^{-2i\pi\underline{\nu}_b}\right)^{-1}\underline{S}_{ba}\ , \tag{17}$$

where the indices a and b refer to the two subspaces of a partitioned $\underline{S}^{cc}$ matrix. Although the above equations do not explicitly involve the open continuum channel, the positions and widths of the autoionizing states are correctly represented owing to the unitarity of the $\underline{S}$ matrix. Since eigenvalues of $\underline{S}$ have absolute value 1, information about the interaction with the continuum is implicitly included in the nonunitarity of the closed-closed $\underline{S}^{cc}$ submatrix.

The above approach is used here to investigate regularities in the spectrum for the final $J = \frac{3}{2}$ states, in the energy range $0.779 \le \hbar\omega \le 0.781$ Ry. Ten weakly closed channels are present, eight of which correspond to the $3s3p\,^3P_{J_c}^o$ thresholds. In the jj-coupled notation introduced above for the channel structure, $|[(L_c,S_c)J_c,(l_o,s_o)j_o]J\rangle$, the eight triplet channels that dominate the dynamics are

$3s3p\,^3P_0^o$: $|[(1,1)0,(1,\frac{1}{2})\frac{3}{2}]\frac{3}{2}\rangle$,

$3s3p\,^3P_1^o$: $|[(1,1)1,(1,\frac{1}{2})\frac{1}{2}]\frac{3}{2}\rangle$, $|[(1,1)1,(1,\frac{1}{2})\frac{3}{2}]\frac{3}{2}\rangle$, $|[(1,1)1,(3,\frac{1}{2})\frac{5}{2}]\frac{3}{2}\rangle$,

$3s3p\,^3P_2^o$: $|[(1,1)2,(1,\frac{1}{2})\frac{1}{2}]\frac{3}{2}\rangle$, $|[(1,1)2,(1,\frac{1}{2})\frac{3}{2}]\frac{3}{2}\rangle$, $|[(1,1)2,(3,\frac{1}{2})\frac{5}{2}]\frac{3}{2}\rangle$, $|[(1,1)2,(3,\frac{1}{2})\frac{7}{5}]\frac{3}{2}\rangle$.

Two other closed channels are attached to a nondegenerate threshold $3s3p\,^1P^o$ and have only a minor effect on the spectrum, since there are no $3s3p(\,^1P)np\,^{2S+1}L^e$ resonances below the $3s3p\,^3P_{J_c}^o$ thresholds. The single-channel subspace a of the partitioned matrix $\underline{S}^{cc}$ in Eq. (17) corresponds to the $|[(1,1)0,(1,\frac{1}{2})\frac{3}{2}]\frac{3}{2}\rangle$ channel (there is only one channel converging to the $3s3p\,^3P_0^o$ threshold), whereas part b contains all other channels, converging to higher thresholds.

Figures 6(a), 6(b), and 7 show universal curves for the real and twice the imaginary parts of μ_0. The latter is just the reduced width function $\Gamma_{\rm red} \equiv \Gamma\nu_0^3 = 2{\rm Im}\mu_0$. These figures also show the quantum defects and reduced widths of the physical resonances obtained by a direct search for maxima of the trace of the time delay matrix (i.e., twice the energy derivative of the eigenphase sum in a.u.). The resulting quantum defect μ_0 oscillates regularly as ν_1 and ν_2 increase with increasing energy. An interesting feature is a "wiggle," that is, a narrow energy range where ${\rm Re}\mu_0$ changes from positive to negative slope. If the ionization threshold with $J_c = 2$ was absent, these wiggles would appear periodically each time ν_1 increased by unity. In this spectrum with three closed channel thresholds nearby, however, the exact periodicity in ν_1 is destroyed by the periodic occurrence in ν_2 of Rydberg perturbers that converge to the threshold $J_c = 2$. Figure 6(b) shows this more clearly on a smaller scale. The occurrence of an energy range where ${\rm Re}\mu_0$ has a negative slope differs from the behavior of typical Lu-Fano

plots which exhibit a strictly increasing phase shift (provided the energy dependence of the $\underline{K}$ matrix is negligible). This type of behavior was earlier identified [15] to be caused by the interaction of broad perturbers with the continuum. Actually, in comparison with Fig. 7 for the reduced-width function, we can see that the wiggles in $\mathrm{Re}\mu_0$ correspond exactly to the positions of the broadest resonances.

Another striking feature in these plots is the presence of near-vanishing-width resonances. Their appearance has nontrivial implications for studies of statistical properties of autoionizing spectra [28–31]. In this case note that all resonances, including those with nearly zero widths, are distributed along the regular $2\mathrm{Im}\mu_0$ curve of Fig. 7. Such extremely narrow resonances are usually observed in a Rydberg series that is perturbed by a diffuse interloper (to use Fano's terminology [32,33]) that is spread over several resonances converging to a lower threshold ($J_c = 0$ in this case). In general, they appear if there is only one open channel (in our studies, there is only one open channel below the $3s3p\,^3P_0^o$ threshold for each final J value, e.g., $[|(0,0)0,(2,\frac{1}{2})\frac{3}{2}]\frac{3}{2}\rangle$) and arise either due to selection rules for the Coulomb autoionization (e.g., if there are LS-forbidden states that cannot directly autoionize) or else owing to destructive interference between the different closed channels. These features are clearly identifiable in the aluminum spectrum in this energy range near the three fine-structure thresholds.

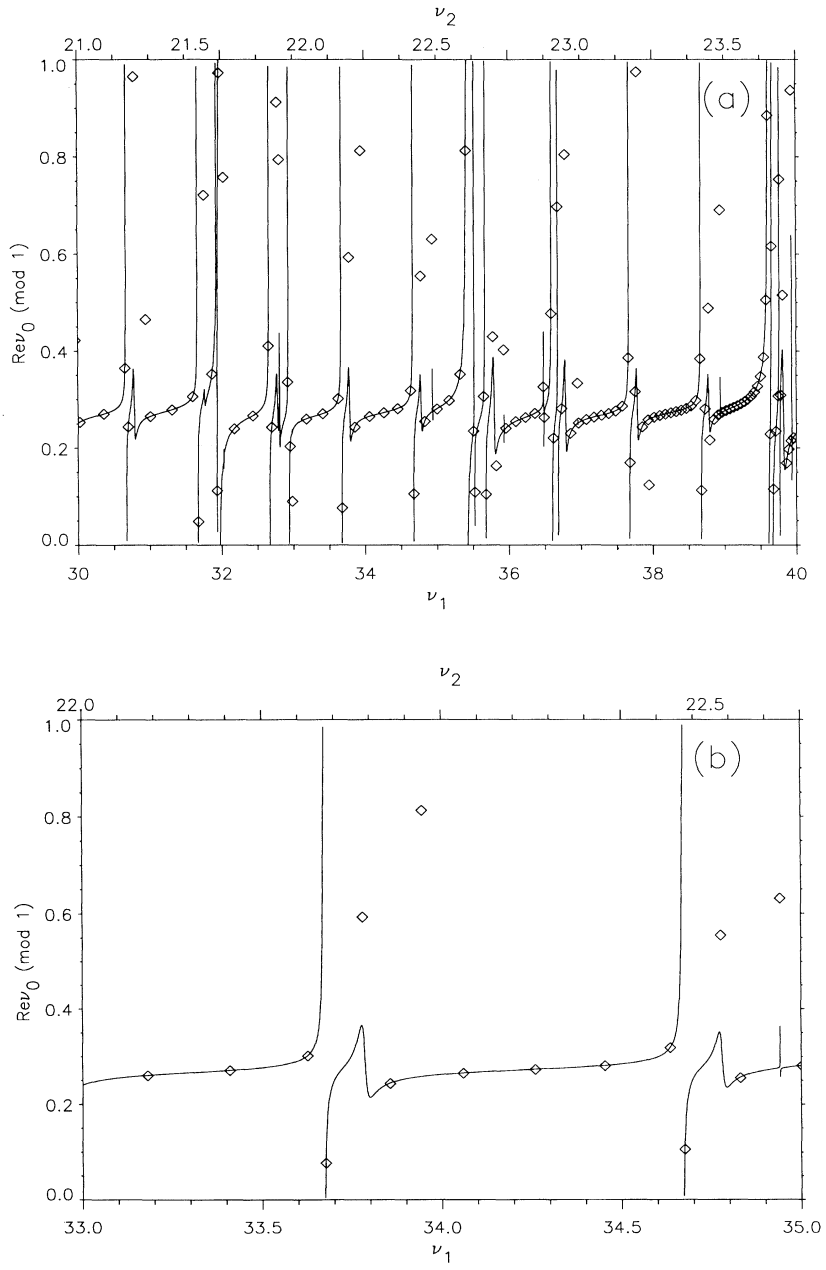

FIG. 6. Quantum defects of resonances (diamonds), which have been obtained by a search for maxima of the energy derivative of the eigenphase sum, are compared in (a) to the real part of the resonance quantum defect ($\mathrm{Re}\mu_0$) (solid line) obtained by solving Eq. (16). The horizontal axes are scaled in units of effective quantum numbers ν_i relative to the $^3P_1^o$ threshold (lower axis) and relative to $^3P_2^o$ (upper axis). In (b) we use a smaller scale of effective quantum numbers to bring out regions of negative slope in quantum defects.

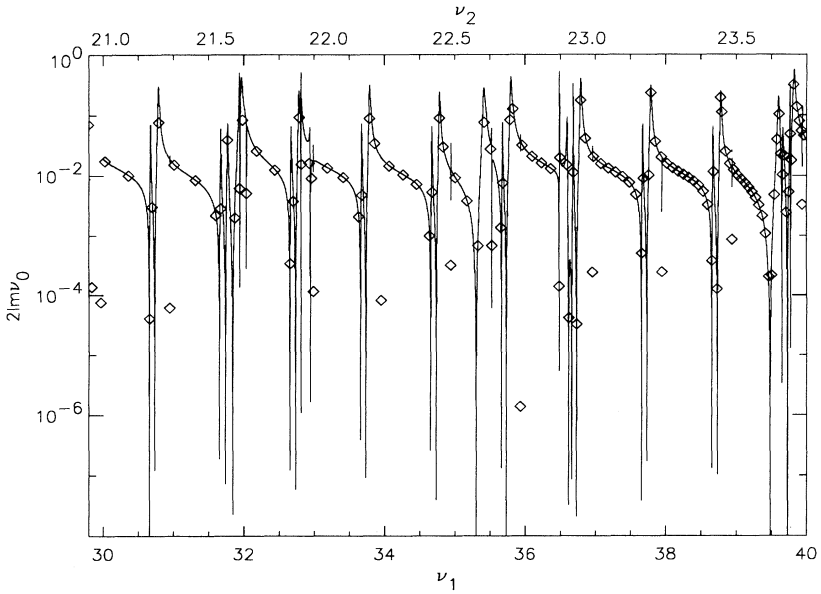

FIG. 7. The reduced widths of resonances (diamonds) obtained from a time-delay analysis are compared to twice the imaginary part of the resonance quantum defect $2\mathrm{Im}\mu_0$ (solid line) obtained by solving Eq. (16). The effective quantum number scales for the upper and lower horizontal axes are the same as in Fig. 6(a).

B. Statistical distribution of resonances

When spectra reach a certain level of complexity they become increasingly difficult to analyze in any conventional (state-by-state) description. This difficulty has stimulated many to abandon all efforts to find regularity in the spectrum and to resort instead to a study of various statistical properties. One of the most widely studied statistical measures is the "nearest-neighbor spacing" (NNS) distribution of the energy differences between successive states in the spectrum, which typically follows a Wigner-type distribution in regions of extreme complexity [16]. A second measure applied to unstable states is the distribution of decay widths, which follows a Porter-Thomas-type distribution in many different cases studied to date [15,30,31]. Spectra that follow these distributions are sometimes viewed as random, in the sense that the Wigner distribution accurately characterizes the distribution of NNS for the eigenvalues of random matrices. The random type of statistical distributions have also been observed to correlate with the onset of chaos in the Newtonian dynamics of some systems. On the other hand, in nonchaotic classical regimes the quantum spectrum tends to exhibit a Poissonian distribution, which in quantum-mechanical terms is associated with weak channel interactions.

The Wigner distribution for the probability $P_W(s)$ of finding two levels separated by a particular spacing s is given by

$$P_W(s) = \frac{\pi s}{2D^2} e^{-\pi s^2/4D^2} , \tag{18}$$

where D is an average spacing and $P_W(s)$ is normalized so that

$$\int sP_W(s)ds = D, \quad \int P_W(s)ds = 1 . \tag{19}$$

One of the characteristics of the NNS distribution is the vanishing probability $P_W(s)$ as $s \to 0$. This is due to the occurrence of diffuse interlopers in the host spectrum which tend to generate strong level repulsion [33]. Because diffuse interlopers are present in the quantum defect plots of Fig. 6, the Wigner energy-level distribution is expected to describe a portion of the aluminum spectrum. The Porter-Thomas distribution for the probability to find a level with an autoionization width Γ is given by the expression

$$P_{\mathrm{PT}}(\Gamma) = (2\pi\Gamma)^{-1/2} e^{-\Gamma/2}, \tag{20}$$

where Γ is expressed in units of an average width. For very narrow resonances, the Porter-Thomas distribution is proportional to $\Gamma^{-1/2}$.

We consider the statistical distributions for the $J = \frac{3}{2}$ final states in the energy range $0.771 \leq \hbar\omega \leq 0.781$ Ry. The region immediately below $3s3p\,^3P_0^o$ and above the highest interloper converging to either $3s3p\,^3P_1^o$ or $3s3p\,^3P_2^o$ is eliminated in these studies because the Rydberg spectrum becomes completely regular. The eight weakly closed channels converging to the three $^3P_{J_c}^o$ thresholds give rise to nearly 300 resonances in the $0.771 \leq \hbar\omega \leq 0.781$ Ry energy range. Since widths decrease with energy in proportion to ν^{-3}, a more proper function to analyze in connection with the Porter-Thomas distribution is the reduced width $\Gamma_{\mathrm{red}} = \Gamma\nu^3$. Γ_{red} brings out the effects of the channel interaction more clearly because it eliminates the strongest energy dependence associated with the trivial normalization factor ${\nu_0}^3$.

To determine the NNS distribution we search for resonances on an energy scale rewritten as in Refs. [15,34], using a "generalized" effective quantum number variable, defined here as $\nu_{\mathrm{gen}} = \nu_0 + 3\nu_1 + 4\nu_2$; the multiplicative constants are the numbers of channels converging to each of the respective $^3P_{J_c}^o$ thresholds. On average, there is

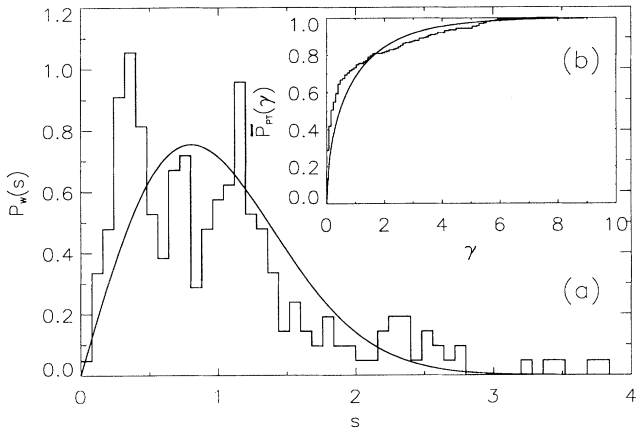

FIG. 8. (a) The NNS statistical distribution of resonances is compared with the analytical Wigner distribution $P_W(s)$ [Eq. (18)], while (b) the cumulative distribution of reduced widths is compared with the Porter-Thomas result $\overline{P}_{\rm PT}(\gamma)$ from Eq. (21).

one more resonance in the spectrum each time $\nu_{\rm gen}$ increases by unity, ensuring that the mean level density, which rescales the variable s in Eq. (18), is very nearly constant on this scale. Figure 8(a) shows the NNS distribution of our resonance level spacings and compares it with the analytical Wigner form (18). The two curves are in fair but not quantitative agreement. Figure 8(b) shows the *cumulative* distribution of widths $\overline{P}_{\rm PT}(\gamma)$, defined in terms of the resonance width density $P_{\rm PT}(\Gamma)$ by

$$\overline{P}_{\rm PT}(\gamma) = \int_0^\gamma P_{\rm PT}(\Gamma) d\Gamma. \tag{21}$$

The cumulative width distribution represents the number of resonances whose widths are smaller than a given width γ. The advantage of using this distribution function is that $\overline{P}_{\rm PT}(\gamma)$ does not diverge as $\gamma \to 0$, in contrast to the Porter-Thomas distribution giving the number of widths between Γ and $\Gamma + d\Gamma$ in Eq. (20). As in the Be example studied by Ref. [15], the agreement between numerical and analytical width distributions is very good, especially in the zero-width limit, and we concur that the Porter-Thomas distribution appears to be more generally applicable to such spectra than is the Wigner NNS distribution.

The viewpoint is frequently offered [29] that agreement of resonance level statistics with Wigner and Porter-Thomas distributions implies the presence of chaos in the system. While chaos is a useful generic property that can be used to classify classical systems, we stress that specific quantum spectra can display simple and clear regularities that emerge, e.g., from the analysis of Sec. IV A above and from the spectra of Be discussed in Ref. [15]. This shows, at the very least, that these two statistical measures cannot characterize complex spectra with any degree of completeness. More specifically, spectra that follow the Wigner and Porter-Thomas distributions can still show striking regularities that cannot be simulated by a random number generator and these regularities are amenable to theoretical interpretation.

V. CONCLUSIONS

The $LS \to jj$ frame transformation enables us to construct semirelativistic photoionization cross sections. The effects of relativity, although most pronounced in the high-energy regime ($n \geq 10$) below the $3s3p\,^3P^o$ threshold, are also important for lower-lying states. The spin-induced interactions mix states belonging to different ^{2S+1}L terms and cause the autoionization of states that would be bound in a strict LS-coupling approximation. The importance of such mixing has been demonstrated by studying in particular the enhancement of decay rates for the $3s3p(\,^3P^o)np\,^2P^e_{3/2}$ states, which even for low n decay much faster than the LS-allowed $3s3p(\,^3P^o)ns\,^2S^e$ series. In addition to the states obtained in previous nonrelativistic calculations, the positions and widths of fine-structure levels of the $np\,^2D^e$, $np\,^2P^e$, and $np\,^4D^e$ series have been determined. The present results are in good overall agreement with experimental works and we also agree with previous theoretical works for those states that can be described without including spin-dependent effects.

The transition from LS to jj coupling for higher energies has been analyzed in the context of statistical distributions. We have shown that the spectra do exhibit a type of chaotic behavior of the level spacing and widths, similar to the Wigner and Porter-Thomas distributions. At the same time, however, the same spectra have striking regularities in the pattern of energy levels and widths including, for example, a periodic occurrence of very long-lived resonances.

ACKNOWLEDGMENTS

The authors would like to thank M. Aymar for extensive discussions. This research is supported by the Division of Chemical Sciences, Office of Basic Energy Sciences, Office of Energy Research, U.S. Department of Energy, Grant No. DE-FG-02-90ER14145.

[1] C.H. Greene, Phys. Rev. A **32**, 1880 (1985).
[2] C.H. Greene, *Fundamental Processes of Atomic Dynamics* (Plenum, New York, 1988), p. 105.
[3] F. Robicheaux and C.H. Greene, Phys. Rev. A **46**, 3821 (1992).
[4] C.M. Lee and K.T. Lu, Phys. Rev. A **8**, 1241 (1973).
[5] C.H. Greene, J. Opt. Soc. Am. B **4**, 775 (1987).
[6] A.W. Weiss, Phys. Rev. A **9**, 1524 (1974).
[7] C.D. Lin, Astrophys. J. **187**, 385 (1974).
[8] P.F. O'Mahony, Phys. Rev. A **32**, 908 (1985).
[9] S.S. Tayal and P.G. Burke, J. Phys. B **20**, 4715 (1987).
[10] M. Le Dourneuf, V.K. Lan, P.G. Burke, and K.T. Taylor,

J. Phys. B **8**, 2640 (1975).
[11] J.L. Kohl and W.H. Parkinson, Astrophys. J. **184**, 661 (1973).
[12] J.M. Esteva, Ph.D. thesis, Centre National de la Recherche Scientifique, 1974, No. A09976 (unpublished).
[13] R.A. Roig, J. Phys. B At. Mol. Phys. **8**, 2939 (1975).
[14] G.K. James, L.F. Forrest, K.J. Ross, and M. Wilson, J. Phys. B **18**, 775 (1985).
[15] C.H. Greene and M. Aymar (unpublished).
[16] T.A. Brody, J. Flores, J.B. French, P.A. Mello, A. Pandey, and S.S.M. Wong, Rev. Mod. Phys. **53**, 385 (1981).
[17] C.H. Greene and L. Kim, Phys. Rev. A **38**, 5953 (1988).
[18] For recent review of MQDT, see M.J. Seaton, Rep. Prog. Phys. **46**, 167 (1983).
[19] M. Aymar, J. Phys. B **23**, 2697 (1990).
[20] W. Johnson, D. Kolb, and K.N. Huang, At. Data Nucl. Data Tables **28**, 333 (1983).
[21] C.E. Moore, *Atomic Energy Levels*, Natl. Bur. Stand. (U.S.) Circ. No. 467 (U.S. GPO, Washington, DC, 1949), Vol. I.
[22] P.-O. Löwdin, Phys. Rev. **97**, 1474 (1055).
[23] C. Froese Fischer, *The Hartree-Fock Methods for Atoms* (Wiley, New York, 1977).
[24] C. Froese Fischer, Comput. Phys. Commun. **64**, 369 (1991).
[25] M. Aymar and C.H. Greene (unpublished).
[26] C.H. Greene and M. Aymar, Phys. Rev. A **44**, 1773 (1991).
[27] K.T. Lu and U. Fano, Phys. Rev. A **2**, 81 (1970).
[28] C. Iu, G.R. Welch, M.M. Kash, L. Hsu, D. Kleppner, D. Delande, and J.C. Gay, Phys. Rev. Lett. **66**, 145 (1991).
[29] B. Grémaud, D. Delande, and J.C. Gay, Phys. Rev. Lett. **70**, 1615 (1993).
[30] G.R. Welch, M.M. Kash, C. Iu, L. Hsu, and D. Kleppner, Phys. Rev. Lett. **62**, 1975 (1989).
[31] C. Iu, G.R. Welch, M.M. Kash, L. Hsu, and D. Kleppner, Phys. Rev. Lett. **63**, 1133 (1989).
[32] U. Fano and A.R.P. Rau, *Atomic Collisions and Spectra* (Academic, Orlando, 1986).
[33] U. Fano, Phys. Rev. A **37**, 4037 (1988).
[34] M. Draeger and H. Friedrich, Phys. Rev. A **44**, 3346 (1991).